A generalised analytical framework for active earth pressure on retaining walls with narrow soil

Lai, Fengwen; Zhang, Ningning; Liu, Songyu; Yang, Dayu

DOI
10.1680/jgeot.21.00305

Publication date
2022

Document Version
Final published version

Published in
Geotechnique

A generalised analytical framework for active earth pressure on retaining walls with narrow soil

FENGWEN LAI*, NINGNING ZHANG†, SONGYU LIU‡ and DAYU YANG§

Active earth pressure on retaining structures supporting a narrow column of soil cannot be properly analysed using Coulomb's theory. Finite-element limit analysis (FELA) shows that the soil forms multiple failure surfaces if the soil column is sufficiently narrow. This paper proposes a framework for active earth pressure estimation for narrow soils by combining an arched differential element method and a sliding wedge method. The analytical framework considers both soil friction and cohesion, soil arching effects and shear stress between adjacent differential elements. The solution obtained is validated against experimental data and FELA results. Through parametric studies, the effects on the active earth pressure of the aspect ratio, soil friction, soil cohesion and wall–soil interface roughness are examined. To facilitate the use of the proposed framework in design, a modified active earth pressure coefficient and an application height of active thrust are provided.

KEYWORDS: analytical approach; earth pressure; finite-element limit analysis; limit equilibrium methods; narrow soil; retaining structure; retaining walls; soil arching

INTRODUCTION

As a common type of geotechnical infrastructure, retaining walls have been widely constructed to maintain the stability of soils behind the retaining structures. When designing a retaining wall, of concern is determining the active earth pressure exerted by the retained soil. The traditional Coulomb and Rankine earth pressure theories have been used widely to estimate the active earth pressure on retaining walls; to improve the accuracy of those theories in design, several analytical approaches based on limit equilibrium theory have also been proposed, such as the differential element method (Paik & Salgado, 2003), the slice method (Zhu & Qian, 2000) and the slip line method (Liu & Wang, 2008). Most of these approaches assume that (*a*) the rupture of the backfill behind a wall involves only one slip surface and (*b*) the failure body is a single intact triangular thrust wedge. However, in some practical cases (e.g. highways in mountainous terrain, backfilled stopes, twin adjacent excavations, excavation near basement walls, excavation near pile groups), as shown in Fig. 1, a retaining wall has to be constructed near an existing structure, thereby limiting the width of the soil behind it. Consequently, the assumed single triangular thrust wedge cannot theoretically form in shape and size, and more than one slip surface is likely to form in the narrow soil behind the retaining wall.

It is essential to understand experimentally the underlying load transfer mechanisms in narrow backfills behind retaining walls. Extensive experimental studies (Frydman & Keissar, 1987; Take & Valsangkar, 2001; O'Neal & Hagerty, 2011) have revealed the non-linear distribution of active earth pressure on retaining walls with narrow granular backfills, which was attributed to the soil arching effect as proposed by Terzaghi (1943). However, because of the complexities involved, the relevant laboratory research has developed comparatively slowly and insufficiently, focusing mostly on purely frictional soils and with very little testing of cohesive soils.

Numerical modelling is a powerful tool for studying the failure mechanism of retained soils and the problem of earth pressure, effectively overcoming the practical difficulties of repeating experimental tests. It can facilitate efficient incorporation of wall movements in the modelling process (Fan & Fang, 2010; Li *et al*., 2017), but the displacement-based finite-element method used for continuum materials and the discrete-element method for granular materials are relatively time-consuming. Instead, the recently developed computer-aided finite-element limit analysis (FELA) (Sloan, 2013) can handle extremely complex boundaries with high efficiency. Benefiting from this advantage, FELA has been used to interpret the failure mechanism of retaining walls with narrow backfill (Chen *et al*., 2019), and the present study also uses the FELA technique to observe the number and shape of slip surfaces in narrow soil.

Analytical approaches have prevailed, benefitting from their advantage of allowing load transfer mechanisms (e.g. soil arching) and failure mechanisms (e.g. number and shape of slip surfaces) to be considered in designs. Frydman & Keissar (1987) suggested the slip line method to determine the earth pressure/thrust on retaining walls with narrow soil; this method estimates relevant centrifuge results satisfactorily, but its complexity limits its wider practical use. To improve the applicability of analytical approaches in narrow retained soils, researchers have presented two representative limit equilibrium methods with relatively simple formulations – namely, the sliding wedge method (Greco, 2013) and the horizontal differential element method (Chen *et al*., 2017). The first method allows complex failure mechanisms with multiple slip surfaces, but it cannot consider properly the principal stress rotation caused by the soil arching effect

Manuscript received 27 September 2021; revised manuscript accepted 30 September 2022.
Discussion on this paper is welcomed by the editor.
* Institute of Geotechnical Engineering, Southeast University, P. R. China; also Faculty of Civil Engineering and Geosciences, Delft University of Technology, the Netherlands (Orcid:0000-0002-9045-0659).
† Institute of Geomechanics and Underground Technology, RWTH Aachen University, Germany (Orcid:0000-0003-3425-8926).
‡ Institute of Geotechnical Engineering, Southeast University, P. R. China (Orcid:0000-0002-8135-3806).
§ Institute of Geotechnical Engineering, Southeast University, P. R. China (Orcid:0000-0002-5811-5690).

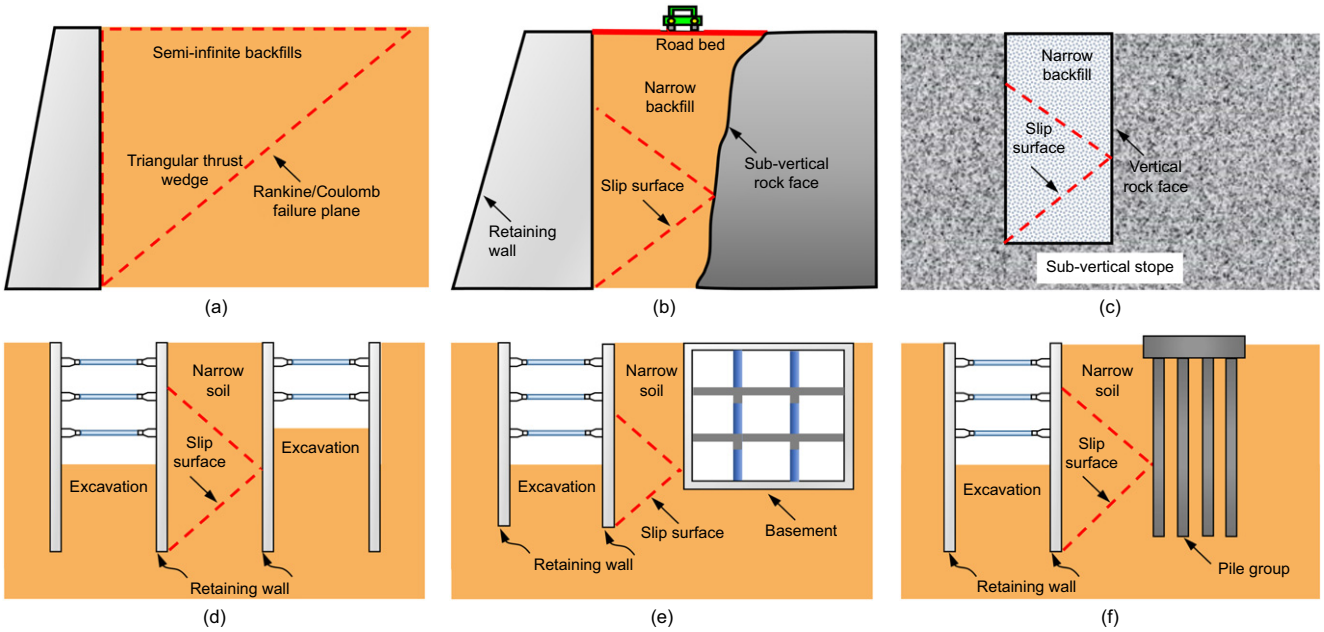

Fig. 1. Examples of retaining walls with narrow soils/backfills: (a) Rankine/Coulomb failure plane in backfills of semi-infinite space; (b) montane highway; (c) backfilled stope; (d) twin adjacent excavations; (e) excavation near basement; and (f) excavation near pile group

(Handy, 1985). By contrast, the differential element method addresses this limitation by discretising the thrust wedge into a number of horizontal elements, but it also has certain limitations: (*a*) horizontal shearing stresses between adjacent elements are always neglected during the integration of horizontal soil elements, which may lead to overestimated earth pressure/thrust (Cao *et al.*, 2020); (*b*) a lateral stress ratio at the wall using the average vertical stress across a given differential element instead of the real vertical stress on the wall has to be introduced to estimate the lateral earth pressure, thereby resulting unavoidably in some deviations from reality (Paik & Salgado, 2003); and (*c*) this method is typically restricted to soils with one slip surface.

The existing analytical approaches were proposed mainly for cohesionless soils, so they cannot be used properly for cohesive soils, such as clays and silts, which are common types of retained soil. Therefore, the objective herein is to propose an analytical framework for determining the active earth pressure on retaining walls with narrow cohesive–frictional soil by way of an overall consideration of soil cohesion, soil arching, horizontal shearing forces between adjacent differential elements and complex failure patterns. The aim of this analytical framework is to introduce a novel method – the arched differential element (ADE) method – to tackle directly the principal stress rotation induced by soil arching and consider the horizontal shearing forces between adjacent elements. The ADE method requires only simple mechanical equilibrium equations to solve for the lateral earth pressure, without the need to introduce the lateral stress ratio that is required in the horizontal differential element method (Paik & Salgado, 2003). The principles of the sliding wedge method are also used to allow for multiple failure surfaces. Overall, the present analytical framework is a generalised one that calculates more accurately the earth pressure exerted by narrow soil behind a retaining wall, benefitting from the artful combination of the sliding wedge method and the ADE method.

The present work is organised as follows. First, FELA models are created to identify the complex active failure mechanisms of the narrow soil behind the wall. Based on that, the calculation model combining the ADE method and the sliding wedge method is established. The active earth pressure, σ_w, the active thrust E_a and its application height z_s are formulated considering soil arching, the horizontal shearing force and multiple slip surfaces. The proposed analytical framework is validated against previously published results and numerical solutions, and the influences of key design parameters on σ_w, E_a and z_s are discussed. Finally, simplified design equations are proposed for practical use.

ACTIVE FAILURE MECHANISMS

Problem definition and FELA model details

FELA is a numerical approach used for limit analysis, combining classical plasticity theorems with finite-element discretisation. Using FELA programs, typical stability problems in geotechnical engineering can be solved quickly, even under complex geometric loading and boundary conditions (Sloan, 2013). In the present study, the state-of-the-art FELA program Optum G2 (Krabbenhoft *et al.*, 2015) is used to obtain the general failure modes of narrow retained soils. In Optum G2, the true collapse load is determined by narrowing the upper bound (UB) and lower bound (LB) plasticity solutions using second-order cone programming.

The active response of narrow soil was studied numerically by means of the problem defined in Fig. 2. Two vertical rigid retaining walls with height H were used to support the homogeneous cohesive–frictional soil with width B. The backfill material in the numerical model was selected as clayey fill with unit weight, γ, cohesion, c, and friction angle, ϕ (Table 1). The clayey backfill under drained conditions was simulated using an elastic, perfectly plastic Mohr–Coulomb (MC) model. The roughness of the wall–soil interface is characterised by a roughness factor μ such that the interface friction angle δ is given by $\tan\delta = \mu\tan\phi$ (Sheil & Templeman, 2022). From the MC failure criterion, the shear strength of the interface satisfies

$$\tau_w = \mu\tau_s = \mu(c + \sigma_w \tan\phi) = \tan\delta(a + \sigma_w) \quad (1)$$

where $a = c\cot\phi$; τ_w and τ_s are the shear strengths of the wall–soil interface and the retained soil, respectively; and σ_w is the normal stress on the interface (the lateral earth pressure

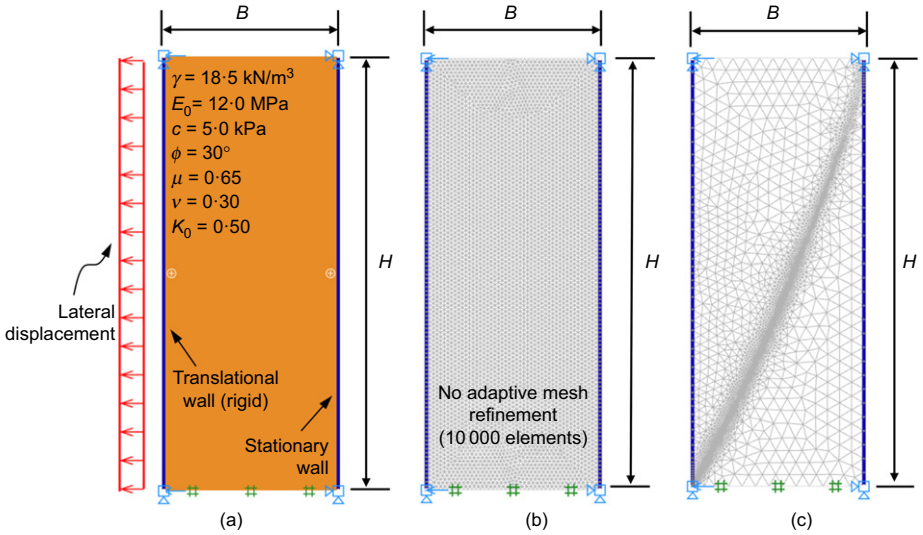

Fig. 2. Finite-element limit analysis under plane-strain condition: (a) numerical model; (b) mesh with no adaptive refinement; and (c) adaptively refined mesh

Table 1. Model parameters of cohesive–frictional soil adopted in FELA

Soil parameter	Value	Reference
Unit weight, γ: kN/m^3	18·5	Data from Chen *et al.* (2016)
Young's modulus, E_0: kPa	12 000	
Poisson's ratio, ν	0·30	
Cohesion, c: kPa	5·0	
Friction angle, ϕ: degrees	30·0	
Wall–soil interface roughness factor, μ: degrees	0·65	
Earth pressure coefficient at rest, K_0	0·50	

on the wall). Herein, μ is also defined as a reduction factor of interface strength.

It is known that FELA inherently employs an associated flow rule that may be unrealistic for soils. However, although previous work (Schmüdderich *et al.*, 2022) has confirmed that the influence of the flow rule (associated or non-associated) on the earth pressure problem may be larger than expected, the present work uses the FELA technique mainly to identify the failure modes for narrow soils. Therefore, the use of associated plasticity is acceptable for numerical observations because the shear band for non-associated material tends to be somewhat more localised than for associated material (Tschuchnigg *et al.*, 2015). The influence of the flow rule on active earth pressure will be discussed further below.

To obtain an active soil failure induced by translational wall movement, the right-side wall was fully fixed, and the left-side wall was allowed to translate only horizontally by prescribing displacements on it. Moreover, the bottom of the soil domain was restrained in both the horizontal and vertical directions, while the top was free. An adaptively refined mesh was generated automatically in FELA to observe the failure modes; during the iterations, an initial mesh with 5000 elements was increased to a final mesh with 10 000 elements after automatic adaptivity.

Observations: shape and number of slip surfaces

Figure 3 presents the FELA observations of the failure mechanism of retaining walls with narrow soil. In Fig. 3(a), three distinct failure mechanisms can be observed: (*a*) if $B/H \geq 0{\cdot}6$, only one triangular thrust wedge with the slip surface initiating from the left-side translational wall base to the backfill surface is present, and the failure mode is referred to as M1; (*b*) if $B/H = 0{\cdot}4$, the slip surface intersects with the right-side wall forming a trapezoidal thrust wedge, and this is denoted as the M2 failure mode; (*c*) if $B/H \leq 0{\cdot}2$, more than one slip surface forms in the narrower backfill space – the first slip surface initiates from the bottom left corner and is reflected by the boundary walls to form more slip surfaces; this mode is defined as M3.

It is well known that soil cohesion plays a vital role in earth pressure problems of retaining structures and determining the plastic yielding zone. However, it has little effect on the shape and number of final slip surfaces of retaining walls with narrow backfills, as demonstrated in Fig. 3(b). In Fig. 3(c), all the scenarios studied in the narrow soil have the M3 failure mode, irrespective of the variation of soil friction angle. This is also seen with the change of roughness factor, except for the fully rough wall–soil interface ($\mu = 1$) where only one slip surface forms (Fig. 3(d)). The shapes of the slip surfaces appear to straighten from a slight arch with both increasing friction angle (Fig. 3(c)) and decreasing roughness factor (Fig. 3(d)). It can also be seen that the sliding angle of the slip surface (α) is relevant mainly to the friction behaviour of backfill materials.

Based on the cases presented in Fig. 3, Table 2 gives the number of slip surfaces induced in narrow cohesive–frictional soils and the corresponding failure mode of more cases covering an extended combination of B/H, ϕ and μ. The influence of soil cohesion – which is negligible as demonstrated in Fig. 3(b) – is not included in Table 2, from which it can also be found that multiple slip surfaces form frequently in a narrower soil column in an active limit state.

The sliding angle can be predicted well using Coulomb's theory (Wang, 2000), as

$$\alpha = \arctan\left(\sqrt{\tan^2\phi + \frac{\tan\phi}{\tan(\phi+\delta)}} + \tan\phi\right) \quad (2)$$

To verify this, equation (2) is used to draw a planar initial slip surface shown by a dashed line with angle α, and a better overlap between the real and predicted slip surfaces can be observed in Fig. 3. Thus, the failure patterns are identified geometrically: M1 for $B/H \geq \cot\alpha$ and M2 or M3 for $B/H < \cot\alpha$.

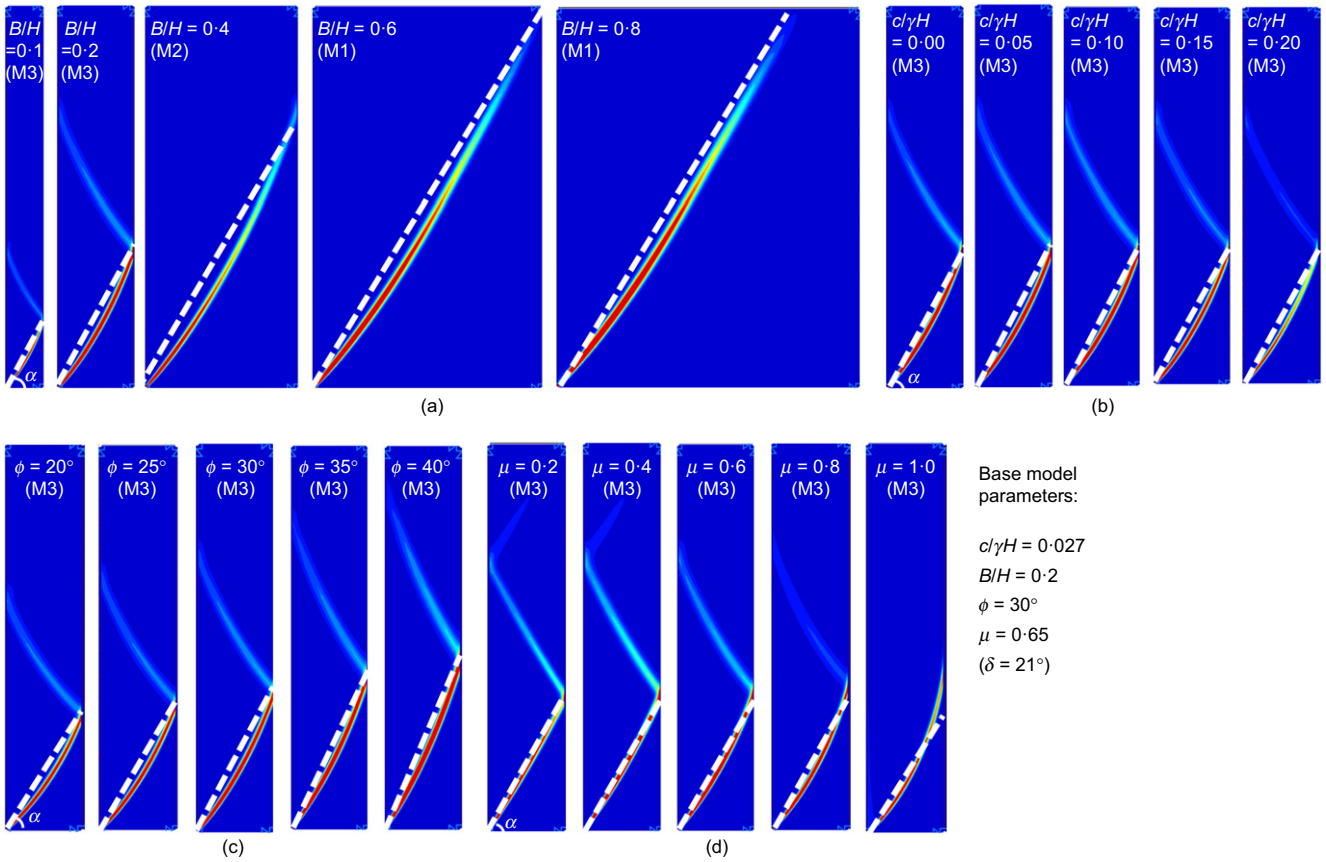

Fig. 3. Failure modes of narrow cohesive–frictional soils under various influencing factors: (a) aspect ratio B/H; (b) dimensionless soil cohesion $c/\gamma H$; (c) soil friction angle ϕ; and (d) wall–soil interface roughness factor μ

Table 2. Number of slip surfaces formed in narrow cohesive–frictional soils

B/H	ϕ: degrees	$\delta = \phi/5$	$\delta = 2\phi/5$	$\delta = 3\phi/5$	$\delta = 4\phi/5$	$\delta = \phi$
0·1	20	5	4	3	2	1
	25	4	4	3	2	1
	30	4	4	3	2	1
	35	4	4	3	2	1
	40	4	3	3	2	1
0·2	20	3	2	2	2	1
	25	2	2	2	2	1
	30	2	2	2	2	1
	35	2	2	2	1	1
	40	2	2	2	1	1
0·4	20	1	1	1	1	1
	25	1	1	1	1	1
	30	1	1	1	1	1
	35	1	1	1	1	1
	40	1	1	1	1	1
0·6	20	1	1	1	1	1
	25	1	1	1	1	1
	30	1	1	1	1	1
	35	1	1	1	1	1
	40	1	1	1	1	1
0·8	20	1	1	1	1	1
	25	1	1	1	1	1
	30	1	1	1	1	1
	35	1	1	1	1	1
	40	1	1	1	1	1

Note: darkest shade = M1, one slip surface with triangular thrust wedge.
Middle shade = M2, one slip surface with trapezoidal thrust wedge.
Lightest shade = M3, multiple slip surfaces.

According to the FELA observations, the shape and number of slip surfaces of narrow cohesive–frictional soils are governed by the aspect ratio, soil friction angle and wall–soil interface friction angle, and are barely affected by soil cohesion. Moreover, the results confirm that multiple slip surfaces (M3) form frequently in narrow soils under active thrust conditions for $B/H < \cot\alpha$, which has to be considered for the routine design of retaining walls with narrow backfills.

Note that although FELA is very fast and efficient for studying the earth-pressure problem, geo-engineers always desire an equally important analytical solution. Therefore, a generalised and design-oriented analytical framework is proposed in the following, which can be used efficiently in the design of retaining walls with narrow cohesive–frictional soils. The FELA results serve as a basis for establishing a sound calculation model and in turn provide validation in the case of cohesive–frictional materials.

PROPOSED ANALYTICAL FRAMEWORK

Calculation model

To consider the complex failure mechanisms of narrow retained soils, a calculation model comprising an upper plugging zone ‘cdef’ with no internal visible shear bands and a lower sliding zone ‘abfe’ with one or more internal shear bands is proposed (Fig. 4). The lower zone allows one or more planar slip surfaces as determined by the sliding wedge method, while the ADE method is used in the upper zone to consider the principal stress rotation induced by the soil arching effect. The interaction between the upper and lower zones requires only imposing the uniform vertical stress obtained from the base of the upper zone on the top of the

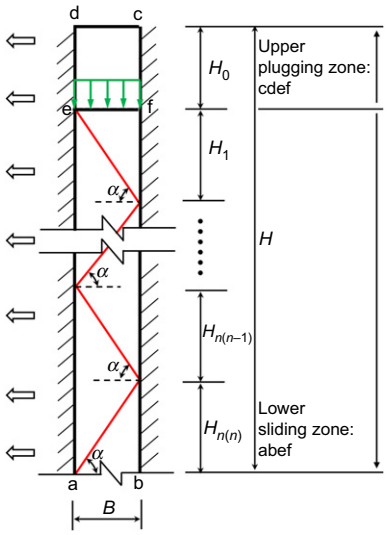

Fig. 4. Calculation model composed of upper plugging zone and lower sliding zone

lower zone, as will be explained fully below. The calculation model involves the following basic assumptions: (*a*) the narrow soil is homogeneous, isotropic and cohesive–frictional, following the MC failure criterion; (*b*) the soil mass retained by the two vertical rigid walls is in a limit equilibrium state; (*c*) the wall displacement is sufficiently large to mobilise fully the strength of the wall–soil interface; (*d*) all the slip surfaces that develop from both the left-side and right-side boundaries are planar and have an identical sliding angle α as predicted by Coulomb's theory (equation (2)) with respect to the horizontal dotted lines inside the soil mass (Fig. 4); (*e*) the full tension cut-off criterion (i.e. negative earth pressure is fully cut off) is used to account for the effect of soil cohesion on the earth pressure, which implicitly means that a crack may form between the wall and the uppermost part of the soil, hence zero earth pressure in the tension zone.

In Fig. 4, H_0 is the height of the upper plugging zone, and H_{nk} is the height of the kth (from top down) of n slip surfaces involved in the lower sliding zone. The geometrical relations give

$$\begin{cases} H_{nk} = B\tan\alpha,\ k \in 1,\ldots,n \\ H_0 = H - nB\tan\alpha \end{cases} \tag{3}$$

For retaining structures, the direction of minor principal stress rotates as induced by soil arching and wall friction, and the major principal stress involved is normal to it, as observed in Fig. 5(a) from the FELA results in the upper zone. Such rotation trajectories of minor principal stress have been described approximately as elliptic, catenary, parabolic, or circular arc shaped curves (Handy, 1985; Paik & Salgado, 2003; Xie & Leshchinsky, 2016). Of these, the circular arc trajectory is widely accepted because of its ease of mathematical description and its better approximation of principal stress rotation (Fig. 5(a)), while the major principal stress involved is applied normal to the circular arc. Therefore, a circular arc curve is used to describe the rotation trajectory of minor principal stress in the proposed framework. More details of minor principal stress rotation in retained soils can be found in Paik & Salgado (2003) and Xie & Leshchinsky (2016).

Upper plugging zone

Figure 5(b) shows further the rotation trajectory of minor principal stress in the theoretical aspect. Accordingly, the rotation trajectory of minor principal stress can be conceptualised as an arched element. Inspired by this concept, the soil domain in the upper zone can be discretised into a finite number of ADEs (see Fig. 5(c)). From a mechanical perspective, only major and minor principal stresses act on the upper and lower boundaries of ADEs. It follows that the horizontal shear stress in soil can inherently be considered in the arched element, which, however, is always neglected when using the horizontal differential element method (Chen *et al.*, 2017).

A force analysis model of the arched soil layer element ($ACC'A'$) with thickness dz at depth z is established in Fig. 5(d). The width B of the element can be expressed as

$$B = 2R_{AC}\cos\theta_{\mathrm{w}} = 2R_{A'C'}\cos\theta_{\mathrm{w}} \tag{4}$$

where both R_{AC} and $R_{A'C'}$ are the radii of the minor principal stress trajectory, and θ_{w} is the angle of the minor principal plane on the wall with respect to the horizontal ($\pi/2 - \theta_{\mathrm{w}}$ corresponds to the rotation angle of the major/minor principal stresses).

The angle θ_{w} in soils can be obtained using

$$\theta_{\mathrm{w}} = \arctan\left[\frac{N - 1 + \sqrt{(N-1)^2 - 4N\tan^2\delta}}{2\tan\delta}\right] \tag{5}$$

where N is the ratio of major to minor principal stress and θ_{w} is required to be within $\pi/2$. The MC failure criterion gives

$$N = \frac{\sigma_1^0 + a}{\sigma_3^0 + a} = \tan^2\left(45° + \frac{\phi}{2}\right) \tag{6}$$

For the detailed formulation process of θ_{w}, refer to Tu & Jia (2014). Fig. 5(a) and equation (5) show that the angle θ_{w} is governed by the soil friction angle and the wall–soil interface friction angle and is independent of the wall depth z. The same applies to R_{AC} and $R_{A'C'}$ from equation (4).

It is assumed that within a specific arched element, the vertical stress σ_{v}^i at an arbitrary point i on the upper boundary arc AC increases linearly with relative buried depth Δz_{Ai}:

$$\sigma_{\mathrm{v}}^i = \sigma_{\mathrm{v}}^0 + \gamma\Delta z_{Ai} \tag{7}$$

where $\Delta z_{Ai} = R_{AC}(\sin\theta_i - \sin\theta_{\mathrm{w}})$ is the relative buried depth between points A and i; θ_i is the rotation angle of minor principal stress at point i; and σ_{v}^0 is the vertical stress on the wall.

Considering the MC failure criterion in combination with Mohr's circle for plane stress (Fig. 6), the vertical stresses σ_{v}^i and σ_{v}^0 can be converted into the major principal stresses σ_1^i and σ_1^0 using

$$(\sigma_1^i + a)C_1^i = \sigma_{\mathrm{v}}^i + a \tag{8}$$

$$(\sigma_1^0 + a)C_1 = \sigma_{\mathrm{v}}^0 + a \tag{9}$$

where

$$C_1^i = \sin^2\theta_i + \frac{\cos^2\theta_i}{N} \tag{10}$$

$$C_1 = \sin^2\theta_{\mathrm{w}} + \frac{\cos^2\theta_{\mathrm{w}}}{N} \tag{11}$$

Substituting equations (8) and (9) into equation (7) gives σ_1^i as

$$\sigma_1^i = \frac{C_1}{C_1^i}\sigma_1^0 + \frac{aC_1 + \gamma(\sin\theta_i - \sin\theta_{\mathrm{w}})R_{AC}}{C_1^i} - a \tag{12}$$

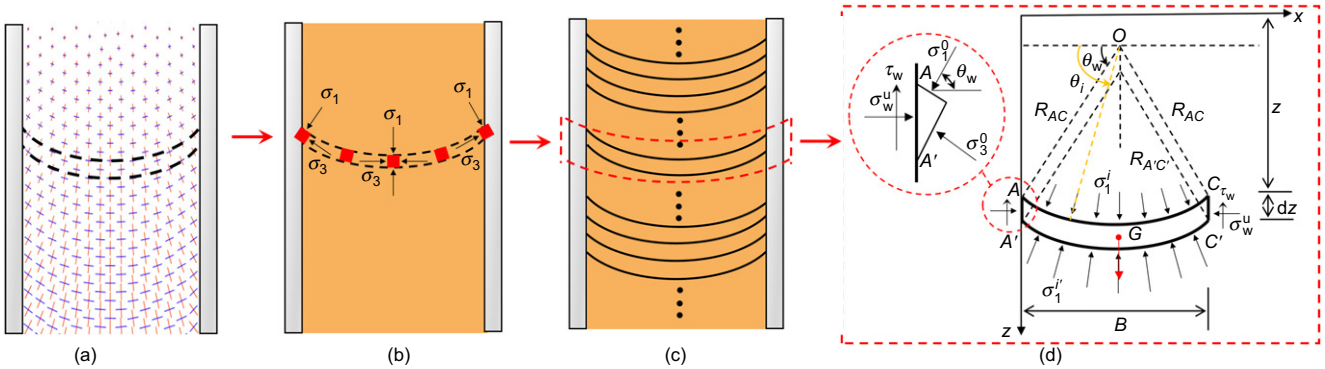

Fig. 5. Calculation model in upper plugging zone: (a) numerical observation principal stress rotation; (b) conceptualisation of arched element along rotation trajectory; (c) discretising narrow soils into arched elements; and (d) force analysis on the arched element

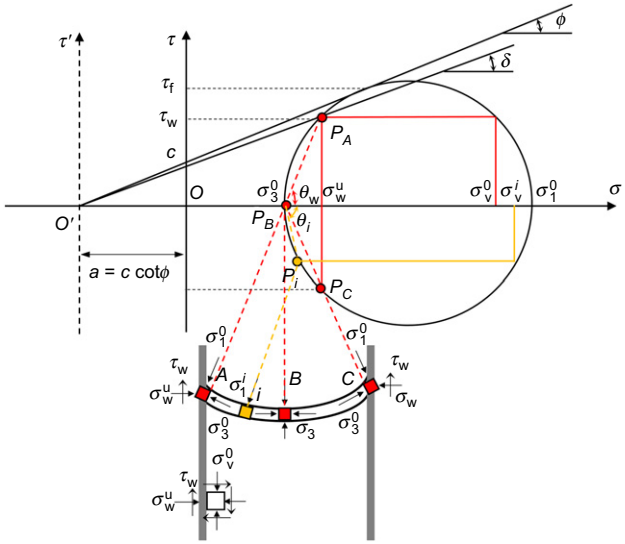

Fig. 6. Mohr circle for stress at various points

For an arched element, only the normal stress σ_1^i is imposed on the upper and lower boundaries AC and $A'C'$, while the normal and tangential stresses are exerted on the lateral boundaries AA' and CC'. It follows that the vertical force acting on the upper boundary arc AC can be obtained by integrating $\sigma_1^i \sin\theta_i$ along the trajectory as

$$F_z^{AC} = 2\int_{\theta_w}^{\pi/2} \sigma_1^i \sin\theta_i R_{AC} \mathrm{d}\theta_i \tag{13}$$

Substituting equation (12) into equation (13) yields

$$F_z^{AC} = C_2 R_{AC}\sigma_1^0 + f(\theta_i)|_{\theta_w}^{\pi/2} \tag{14}$$

where C_2 and $f(\theta_i)|_{\theta_w}^{\pi/2}$ are

$$C_2 = C_1\sqrt{\frac{N}{N-1}}\ln\left[\frac{1+\cos\theta_w\sqrt{(N-1)/N}}{1-\cos\theta_w\sqrt{(N-1)/N}}\right] \tag{15}$$

$$\begin{aligned} f(\theta_i)|_{\theta_w}^{\pi/2} &= 2\int_{\theta_w}^{\pi/2}\left[\frac{C_1 a+\gamma(\sin\theta_i-\sin\theta_w)R_{AC}}{C_1^i}-a\right]R_{AC}\sin\theta_i \mathrm{d}\theta_i \\ &= 2\gamma R_{AC}^2\left[\frac{\pi(1-\sqrt{N})}{2(1-N)}-\frac{N\theta_w-\sqrt{N}\arctan(\sqrt{N}\tan\theta_w)}{1-N}\right] \\ &\quad -\frac{\gamma\sin\theta_w C_2 R_{AC}^2}{C_1}-a\cos\theta_w R_{AC} \end{aligned} \tag{16}$$

Similarly, the vertical force acting on the lower boundary arc $A'C'$ can be given as

$$F_z^{A'C'} = C_2 R_{A'C'}(\sigma_1^0+\mathrm{d}\sigma_1^0) + f(\theta_i')|_{\theta_w}^{\pi/2} \tag{17}$$

and herein $f(\theta_i')_{\theta_w}^{\pi/2} = f(\theta_i)|_{\theta_w}^{\pi/2}$ because $R_{A'C'} = R_{AC}$.

Because of the symmetry, the vertical forces on the lateral boundaries AA' and CC' can be determined as

$$F_z^{AA'} = F_z^{CC'} = \tau_w \mathrm{d}z \tag{18}$$

and the total gravity of the arched element can be expressed as

$$G = \gamma B \mathrm{d}z \tag{19}$$

According to the vertical equilibrium of one arched soil layer element, the following governing equation can be established

$$F_z^{A'C'} - F_z^{AC} + F_z^{AA'} + F_z^{CC'} = G \tag{20}$$

Substituting equations (4), (14) and (17)–(19) into equation (20) leads to

$$\frac{\mathrm{d}\sigma_1^0}{\mathrm{d}z} + \frac{4C_3\cos\theta_w\tan\delta}{C_2 B}\sigma_1^0 + \frac{(4C_3\mu c - 2\gamma B)\cos\theta_w}{C_2 B} = 0 \tag{21}$$

where

$$C_3 = \cos^2\theta_w + \frac{\sin^2\theta_w}{N} \tag{22}$$

Considering $\sigma_1^0 = 0$ at $z = 0$, the major principal stress on the interface for an ADE at depth z can be obtained as

$$\sigma_1^0 = \frac{C_5}{C_4}\left(\mathrm{e}^{-C_4 z}-1\right) \tag{23}$$

where

$$C_4 = \frac{4C_3\cos\theta_w\tan\delta}{C_2 B} \tag{24}$$

$$C_5 = \frac{(4C_3\mu c - 2\gamma B)\cos\theta_w}{C_2 B} \tag{25}$$

Mohr's stress circle gives

$$\sigma_w^u = C_3(\sigma_1^0 + a) - a \tag{26}$$

and the active earth pressure against the wall in the upper plugging zone can be determined by substituting equation (23) into equation (26) to give

$$\sigma_{\mathrm{w}}^{\mathrm{u}} = \frac{C_3 C_5}{C_4}\left(\mathrm{e}^{-C_4 z} - 1\right) + a(C_3 - 1) \tag{27}$$

Lower sliding zone

Figure 4 presents a calculation model for the lower sliding zone, obtained by imposing a vertical resultant force F_z that can be discretised into the average uniform vertical stress $\bar{\sigma}_{\mathrm{v0}}$ on the top to correlate with the upper plugging zone. Therefore

$$\bar{\sigma}_{\mathrm{v0}} = \bar{\sigma}_{\mathrm{v}}|_{z=H_0} = \frac{F_z}{B} \tag{28}$$

is defined in the model.

Based on the sliding wedge method, Fig. 7 shows the force analysis of the sliding zone with one slip surface ($n = 1$).

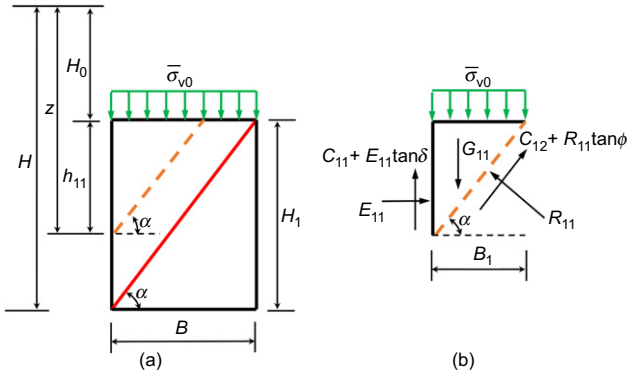

Fig. 7. Calculation model in sliding zone for $n = 1$: (a) geometric configuration; (b) forces acting on wedge W_{11}

The dotted and solid lines represent the hypothetical and real slip surfaces, respectively. The equilibrium equations for the active thrust wedge W_{11} at arbitrary depth z can be established using the sliding wedge method:

$$\begin{cases} E_{11} + (C_{12} + R_{11}\tan\phi)\cos\alpha - R_{11}\sin\alpha = 0 \\ C_{11} + E_{11}\tan\delta + (C_{12} + R_{11}\tan\phi)\sin\alpha + R_{11}\cos\alpha - G_{11} - \bar{\sigma}_{\mathrm{v0}}B_1 = 0 \end{cases} \tag{29}$$

Thus, the resultant force on the wall for wedge W_{11} can be solved for as

$$E_{11} = \frac{\cos\delta[(\bar{\sigma}_{\mathrm{v0}}B_1 + G_{11} - C_{11})\sin(\alpha - \phi) - C_{12}\cos\phi]}{\cos(\alpha - \phi - \delta)} \tag{30}$$

where $G_{11} = \gamma B_1 h_{11}/2$, $C_{11} = \mu c h_{11}$, $C_{12} = c h_{11}/\sin\alpha$, $B_1 = h_{11}/\tan\alpha$, $h_{11} = z + B\tan\alpha - H$ and $H_0 = H - B\tan\alpha$.

Figure 8 shows the force analysis of the sliding zone with two slip surfaces ($n = 2$). Similarly, the equilibrium conditions for the forces on wedges W_{21} and W_{22} are

$$\begin{cases} E_{21} + (C_{22} + R_{21}\tan\phi)\cos\alpha - R_{21}\sin\alpha = 0 \\ C_{21} + E_{21}\tan\delta + (C_{22} + R_{21}\tan\phi)\sin\alpha + R_{21}\cos\alpha - G_{21} - \bar{\sigma}_{\mathrm{v0}}B_2 = 0 \\ E_{22} + (C_{22} + R_{21}\tan\phi)\cos\alpha + (C_{24} + R_{22}\tan\phi)\cos\alpha - R_{21}\sin\alpha - R_{22}\sin\alpha = 0 \\ C_{23} + E_{22}\tan\delta + (C_{24} + R_{22}\tan\phi)\sin\alpha + R_{22}\cos\alpha - (C_{22} + R_{21}\tan\phi)\sin\alpha - R_{21}\cos\alpha - \bar{\sigma}_{\mathrm{v0}}(B - B_2) - G_{22} = 0 \end{cases} \tag{31}$$

Equation (31) makes it possible to solve for the resultant forces on the wall for wedges W_{21} and W_{22} as

$$\begin{cases} E_{21} = \dfrac{\cos\delta[(\bar{\sigma}_{\mathrm{v0}}B_2 + G_{21} - C_{21})\sin(\alpha - \phi) - C_{22}\cos\phi]}{\cos(\alpha - \phi - \delta)} \\ E_{22} = \dfrac{\cos\delta[(\bar{\sigma}_{\mathrm{v0}}B + G_{22} + G_{21} - C_{23} - C_{21})\sin(\alpha - \phi) - C_{24}\cos\phi + E_{21}\cos(\alpha - \phi + \delta)]}{\cos(\alpha - \phi - \delta)} \end{cases} \tag{32}$$

where $G_{21} = \gamma B_2 h_{21}/2$, $C_{21} = uch_{11}$, $C_{22} = ch_{21}/\sin\alpha$, $B_2 = h_{21}/\tan\alpha$, $h_{21} = z + B\tan\alpha - H$, $G_{22} = \gamma(Bh_{21} + Bh_{22}/2 - B_2 h_{21}/2)$, $C_{23} = \mu c(h_{21} + h_{22})$, $C_{24} = ch_{22}/\sin\alpha$, $h_{22} = B/\tan\alpha$ and $H_0 = H - 2B\tan\alpha$.

Figure 9 shows the force analysis of the sliding zone with three slip surfaces, from which the equilibrium conditions for the resultant forces on the wall for wedges W_{31}, W_{32} and W_{33} can be expressed as

$$\begin{cases} E_{31} + (C_{32} + R_{31}\tan\phi)\cos\alpha - R_{31}\sin\alpha = 0 \\ C_{31} + E_{31}\tan\delta + (C_{32} + R_{31}\tan\phi)\sin\alpha + R_{31}\cos\alpha - G_{31} - \bar{\sigma}_{\mathrm{v0}}B_3 = 0 \\ E_{32} + (C_{32} + R_{31}\tan\phi)\cos\alpha + (C_{34} + R_{32}\tan\phi)\cos\alpha - R_{31}\sin\alpha - R_{32}\sin\alpha = 0 \\ C_{33} + E_{32}\tan\delta + (C_{34} + R_{32}\tan\phi)\sin\alpha + R_{32}\cos\alpha - (C_{32} + R_{31}\tan\phi)\sin\alpha - R_{31}\cos\alpha - \bar{\sigma}_{\mathrm{v0}}(B - B_3) - G_{32} = 0 \\ E_{33} + (C_{34} + R_{32}\tan\phi)\cos\alpha + (C_{36} + R_{33}\tan\phi)\cos\alpha - R_{32}\sin\alpha - R_{33}\sin\alpha = 0 \\ C_{35} + E_{33}\tan\delta + (C_{36} + R_{33}\tan\phi)\sin\alpha + R_{33}\cos\alpha - R_{32}\cos\alpha - (C_{34} + R_{32}\tan\phi)\sin\alpha - G_{33} = 0 \end{cases} \tag{33}$$

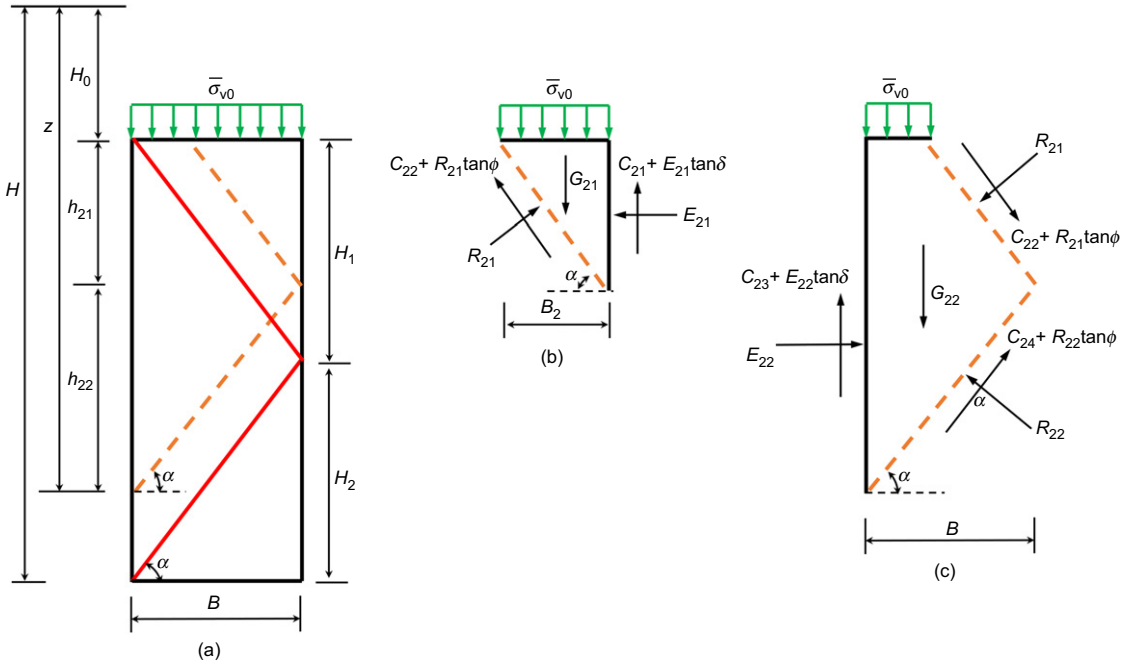

Fig. 8. Calculation model in sliding zone for $n = 2$: (a) geometric configuration; (b) forces acting on wedge W_{21}; (c) forces acting on wedge W_{22}

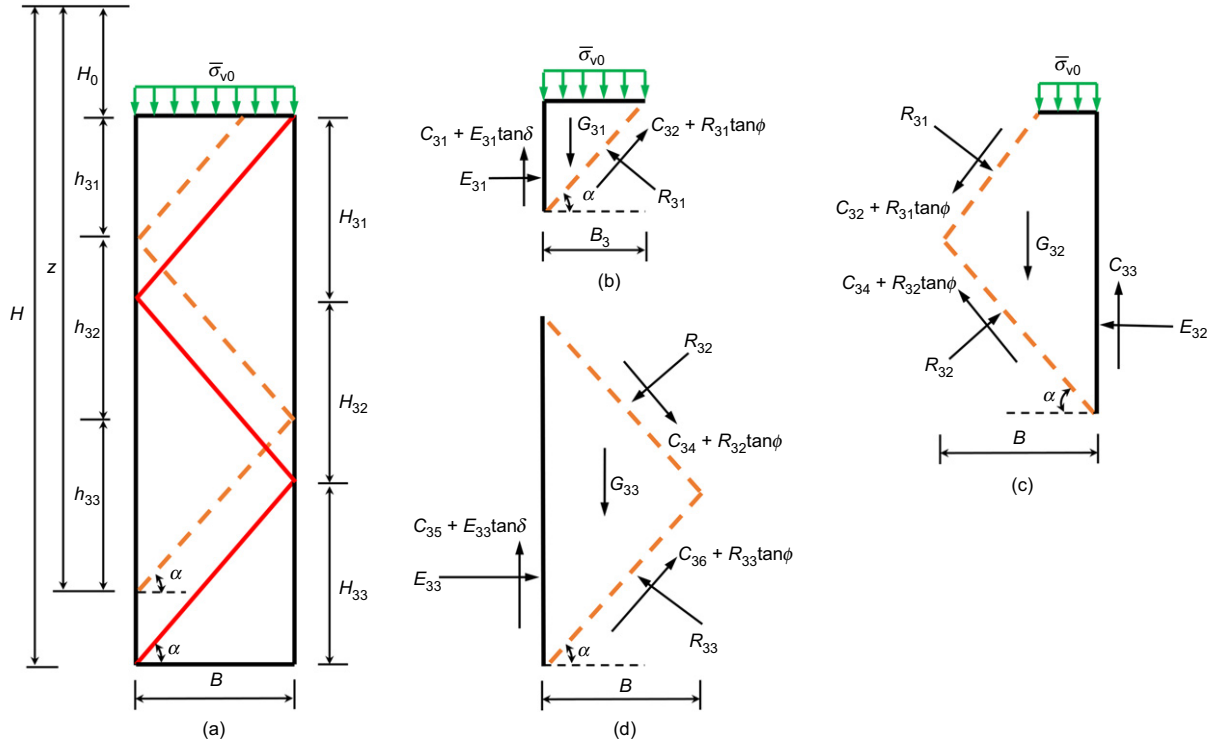

Fig. 9. Calculation model in sliding zone for $n = 3$: (a) geometric configuration; (b) forces acting on wedge W_{31}; (c) forces acting on wedge W_{32}; (d) forces acting on wedge W_{33}

The resultant forces on the wall for the wedges can be obtained by solving equation (33)

where $G_{31} = \gamma B_3 h_{31}/2$, $B_3 = h_{31}/\tan\alpha$, $C_{31} = \mu c h_{31}$, $C_{32} = ch_{31}/\sin\alpha$, $G_{32} = \gamma(Bh_{31} + Bh_{32}/2 - B_3 h_{31}/2)$, $C_{33} =$

$$\begin{cases} E_{31} = \dfrac{\cos\delta[(\bar{\sigma}_{v0}B_3 + G_{31} - C_{31})\sin(\alpha-\phi) - C_{32}\cos\phi]}{\cos(\alpha-\phi-\delta)} \\ E_{32} = \dfrac{\cos\delta[(\bar{\sigma}_{v0}B + G_{31} + G_{32} - C_{31} - C_{33})\sin(\alpha-\phi) - C_{34}\cos\phi + E_{31}\cos(\alpha-\phi+\delta)]}{\cos(\alpha-\phi-\delta)} \\ E_{33} = \dfrac{\cos\delta[(\bar{\sigma}_{v0}B + G_{31} + G_{32} + G_{33} - C_{33} - C_{35})\sin(\alpha-\phi) - C_{36}\cos\phi + E_{32}\cos(\alpha-\phi+\delta)]}{\cos(\alpha-\phi-\delta)} \end{cases} \quad (34)$$

$\mu c(h_{31}+h_{32})$, $C_{34}=ch_{32}/\sin\alpha$, $G_{33}=\gamma Bh_{33}/2$, $C_{35}=\mu c(h_{31}+h_{32}+h_{33})$, $C_{36}=ch_{33}/\sin\alpha$, $h_{31}=z+B\tan\alpha-H$, $h_{32}=h_{33}=B\tan\alpha$ and $H_0=H-3B\tan\alpha$.

As defined, k is the kth slip surface in the sliding zone with n slip surfaces from the top down, thus $1\le k\le n$. Using the recurrence method and combining equations (29)–(34) gives the resultant forces on the retaining wall for wedges formed in the sliding zone for all cases

(a) when $k=1$

$$E_{n1}=\frac{\cos\delta[(\bar{\sigma}_{v0}B_n+G_{n1}-C_{n1})\sin(\alpha-\phi)-C_{n2}\cos\phi]}{\cos(\alpha-\phi-\delta)} \tag{35}$$

where $G_{n1}=\gamma B_n h_{n1}/2$, $C_{n1}=ah_{n1}\tan\delta$, $C_{n2}=ch_{n1}/\sin\alpha$, $B_n=h_{n1}/\tan\alpha$ and $h_{n1}=z+B\tan\alpha-H$

(b) when $k\ge 2$

$$E_{nk}=\frac{\cos\delta\left[\left(\bar{\sigma}_{v0}B+\sum_{i=1}^{k}G_{ni}-C_{n(2k-3)}-C_{n(2k-1)}\right)\sin(\alpha-\phi)-C_{n(2k)}\cos\phi+E_{n(k-1)}\cos(\alpha-\phi+\delta)\right]}{\cos(\alpha-\phi-\delta)} \tag{36}$$

where

$$\sum_{i=1}^{k}G_{ni}=\gamma B\left(\sum_{i=1}^{k-1}(h_{ni})+\frac{h_{nk}}{2}\right) \tag{37}$$

$$h_{nk}=B\tan\alpha \tag{38}$$

All the formulas for the resultant cohesion on the wedges illustrated in Figs 7–9 are summarised as follows

$$\begin{cases} C_{21}=\mu ch_{21} \\ C_{23}=a(h_{21}+h_{22})\tan\delta \\ C_{24}=ch_{22}/\sin\alpha \\ C_{31}=\mu ch_{31} \\ C_{33}=\mu c(h_{31}+h_{32}) \\ C_{35}=\mu c(h_{31}+h_{32}+h_{33}) \\ C_{36}=ch_{33}/\sin\alpha \end{cases} \tag{39}$$

Again, using the recurrence method gives

$$\begin{cases} C_{n(2k-1)}=\mu c\sum_{i=1}^{k}(h_{ni}) & k\in(1,\ n) \\ C_{n(2n)}=ch_{nn}/\sin\alpha \end{cases} \tag{40}$$

Substituting equations (37), (38) and (40) into equation (36) gives

$$E_{nk}=\frac{\cos\delta}{\cos(\alpha-\phi-\delta)}\left\{\begin{array}{l}\left\{\bar{\sigma}_{v0}B+\gamma B\left[z-H+\left(k-\frac{1}{2}\right)B\tan\alpha\right]-a[2z-2H+(2k-1)B\tan\alpha]\right\}\sin(\alpha-\phi) \\ -c\dfrac{B\cos\phi}{\cos\alpha}+E_{n(k-1)}\cos(\alpha-\phi+\delta)\end{array}\right\} \tag{41}$$

In the above analyses, using the sliding wedge method gives the formulas for the resultant forces on thrust wedges in retained soil with any number of slip surfaces. Subsequently, the finite-difference theorem must be used to solve for the lateral active earth pressure on the retaining wall in the lower sliding zone, as shown in Fig. 10. The lower sliding zone is divided into m inclined slices of equal thickness Δz; the ith soil slice is abbreviated as $P_{i-1}P_i$, where the subscript i is the slice number. If the active thrusts exerted by soil slices P_0P_{i-1} and P_0P_i are E_a^{i-1} and E_a^i, respectively, then the active thrust ΔE_a^i on soil slice $P_{i-1}P_i$ can be expressed as

$$\Delta E_a^i=E_a^i-E_a^{i-1} \tag{42}$$

where $E_a^i=E_{nk}(z_i)$, $z_i=i\Delta z$ and $\Delta z=(H-H_0)/m$. Accordingly, the active earth pressure on retaining walls distributed in a sliding zone can be calculated using

$$\sigma_{wi}^{l}=\frac{\Delta E_a^i}{\Delta z} \tag{43}$$

To calculate E_a^i on soil slice P_0P_i at arbitrary depth z in the sliding zone, a hypothetical calculation model is presented in Fig. 11. Each inclined soil element comprises two postulated slip surfaces, which according to the studied active failure mechanism are assumed to be extended in the form of reflections. It follows that equations (35) and (41) can be used directly to obtain $E_{nk}(z_i)$ at arbitrary depth z in the sliding zone.

Finally, the variable $\bar{\sigma}_{v0}$ (or F_z) acting on the top of the sliding zone can be determined using $\sigma_w^u=\sigma_{wi}^l$ at $z=H_0$. The solutions for the earth pressure in the upper and lower zones can be given using the ADE method and the sliding wedge method, respectively.

Active thrust and height of application point

Determining the magnitude and application point of active thrust is fundamental because without them, it is impossible to assess the stability of the retaining wall system against overturning. The magnitude of active thrust on a retaining wall with narrow cohesive–frictional soil can be calculated using

$$E_a=\int_0^{H_0}\sigma_w^u\mathrm{d}z+\sum_{i=1}^{m}\sigma_{wi}^{l}\Delta z \tag{44}$$

which can be rewritten in a dimensionless form as

$$K_a=\frac{2E_a}{\gamma H^2} \tag{45}$$

where K_a is defined as the active thrust coefficient (the active earth pressure coefficient in the framework of Coulomb's theory).

The height z_s from the application point of active thrust to the wall base is given by calculating the moment about the wall base

$$z_s = \frac{\int_0^{H_0} \sigma_w(H-z)\mathrm{d}z + \sum_{i=1}^{m} \sigma_{wi}[H - H_0 - (i-0{\cdot}5)\Delta z]\Delta z}{E_a} \quad (46)$$

In the proposed framework, the input variables are $c/\gamma H$, ϕ, μ and B/H, while the output variables are σ_w (the earth pressure at any wall depth), E_a (or K_a) and z_s.

COMPARISON AND VALIDATION

Purely frictional soil

For validation, the proposed solutions are compared with results from previously reported centrifuge tests, finite-element modelling and analytical solutions in terms of $\sigma_w/\gamma H$ on retaining walls supporting purely frictional backfills ($B/H = 0{\cdot}235$) (Fig. 12(a)). Frydman & Keissar (1987) conducted several groups of centrifuge tests at 43·7g in narrow granular soils to measure the active earth pressure on retaining walls, which can be used as the benchmark for comparison; also, they used stress characteristic solutions and Janssen's silo formula (Janssen, 1895) for comparison. Based on the prototype dimensions of the centrifuge test in Frydman & Keissar (1987), Fan & Fang (2010) provided numerical solutions for the active earth pressure against retaining walls with $B/H = 0{\cdot}235$. Furthermore, considering one, two and three planar slip surfaces, Greco (2013) presented analytical solutions using only the sliding wedge method without considering load transfer mechanisms (e.g. soil arching, horizontal shearing forces).

Figure 12(a) shows that the proposed solutions agree well with the results from centrifuge tests, finite-element modelling and stress characteristic solutions and so are highly accurate for predicting $\sigma_w/\gamma H$ on retaining walls with narrow backfills. The difference between the proposed analytical solutions and those due to Greco (2013) indicates that considering load transfer mechanisms in narrow soils behind retaining walls is necessary for calculating accurately the earth pressure on a wall with limited backfill space. Although Janssen's solution matches the proposed solution well in the upper plugging zone, there are significant variations in the lower sliding zone; this is mainly because Janssen's solution cannot consider some significant factors (e.g. slip surface, horizontal shear force) and so is preferable for estimating at-rest pressure, as noted by Frydman & Keissar (1987).

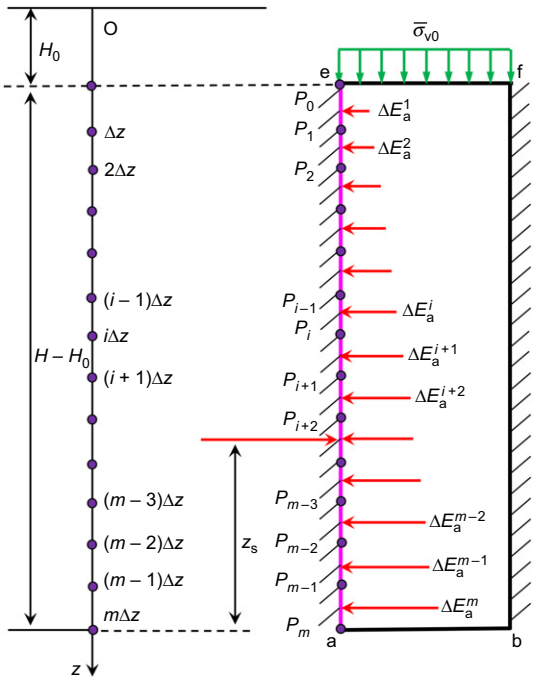

Fig. 10. Division of the thrust plane in sliding zone into m slices and relevant force distribution

Cohesive–frictional soil with non-associativity or associativity

To date, there are no reported tests or measured data for retaining walls with narrow cohesive–frictional soil, so the proposed analytical framework for calculating earth pressure was further compared and verified with numerical solutions using the FELA model parameters given in Table 1. However, an immediate comparison between analytical results and FELA solutions with the associated flow rule ($\psi = \phi$) is somewhat unconvincing because $\psi = \phi$ may be unrealistic for soils, and the soil dilation angle ψ may influence the earth pressure. To consider the non-associated flow rule ($\psi \neq \phi$) in the FELA model as much as possible, the so-called Davis approach (Davis, 1968) with the reduced

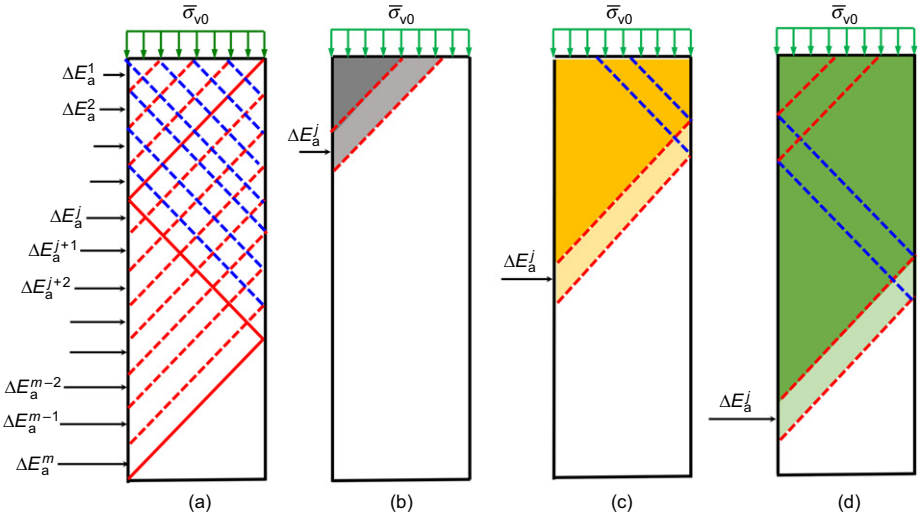

Fig. 11. Method of solving earth pressure distribution in sliding zone based on finite-difference theory: (a) discretisation by assumed slip surfaces for $n = 3$; (b) calculation model for $k = 1$; (c) calculation model for $k = 2$; (d) calculation model for $k = 3$

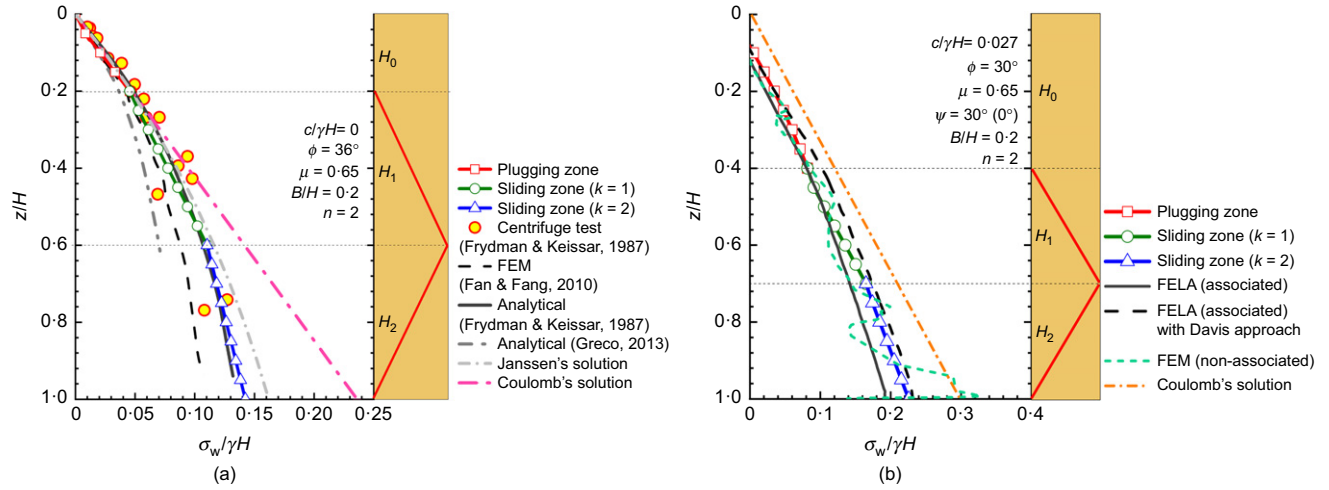

Fig. 12. Validation of earth pressure from the proposed analytical framework in: (a) purely frictional soil; (b) cohesive–frictional soil (note: FEM, finite-element model)

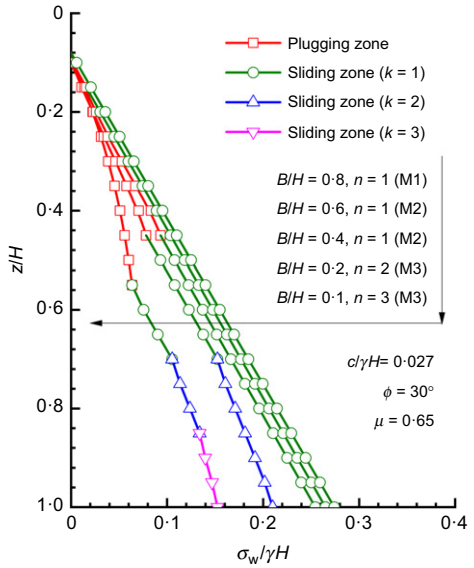

Fig. 13. Effect of aspect ratio on active earth pressure distribution with depth

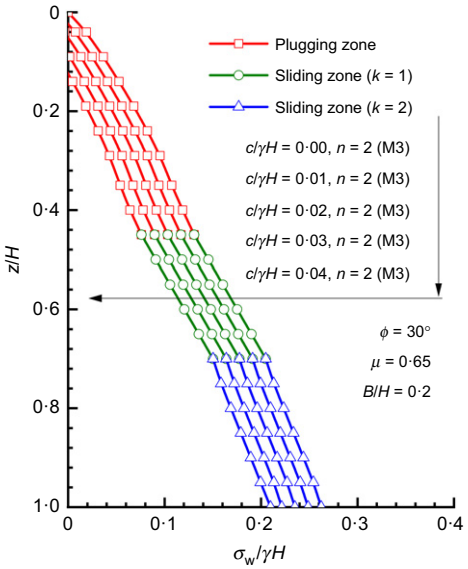

Fig. 14. Effect of normalised soil cohesion on active earth pressure distribution with depth

strength parameters as input ($c^* = 4{\cdot}33$ kPa, $\phi^* = 26{\cdot}6°$) is considered as an alternative to remedy the aforementioned problem. To understand the significance of the flow rule more thoroughly, displacement-based finite-element modelling results considering non-associated plasticity are also presented here. Note that the full tension cut-off criterion was used in all the numerical models performed, which is in line with the proposed framework.

Figure 12(b) shows comprehensive comparisons of the normalised active earth pressure $\sigma_w/\gamma H$ exerted by cohesive–frictional soils on retaining walls. As can be seen, the finite-element modelling results following the non-associated flow rule fit well with those of LB-FELA following the associated flow rule in the upper plugging zone, while there is a small gap in the lower sliding zone. The lower soil dilation angle yields higher active earth pressure values in the lower zone, and the Davis approach also reflects a similar effect. However, the comparison shows that the impact of the dilation angle is not as significant as expected for the active earth pressure in narrow soils, which is also supported by the finite-element modelling results. Note that the finite-element model simulation with the non-associated flow rule exhibited numerical instability, hence the oscillating curve of earth pressure with depth; such numerical oscillations are a consequence of the non-associated flow rule. The comparison in Fig. 12(b) confirms that this drawback can be remedied to some extent with a simple modification of the FELA model with the Davis approach.

As can also be seen, the solutions from the proposed analytical framework for cohesive–frictional soils agree well with the LB-FELA solutions, thereby supporting the validity of the proposed analytical framework in cohesive–frictional soils. Moreover, the comparison indicates that the proposed analytical framework can characterise well the effect of soil cohesion on the active earth pressures on a retaining wall with a limited backfill space.

PARAMETRIC STUDY

Effect of aspect ratio

Figure 13 plots the distribution of normalised active earth pressure $\sigma_w/\gamma H$ with wall depth z/H for various values of

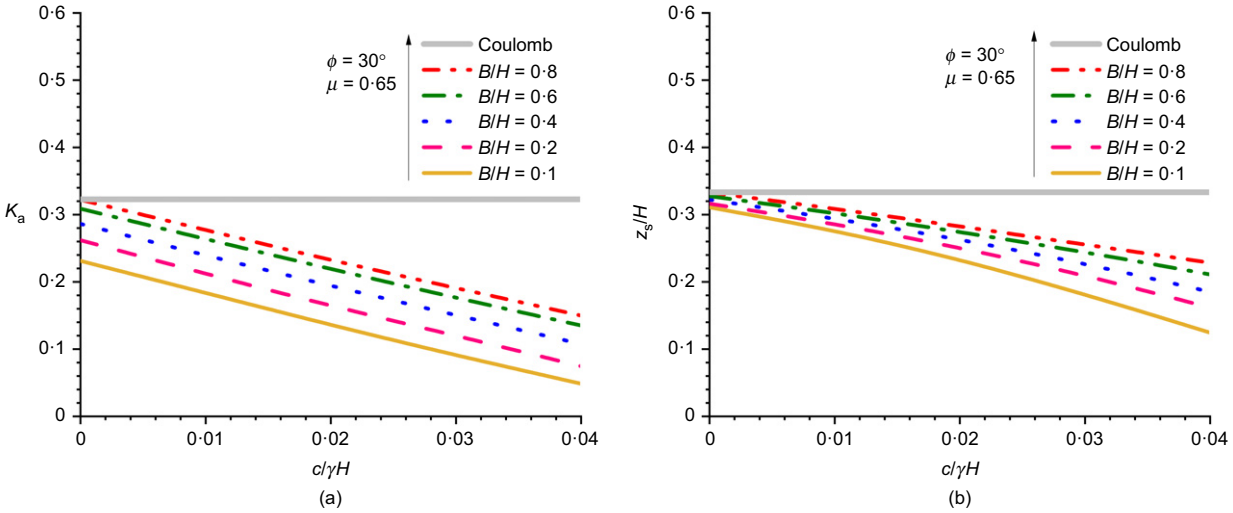

Fig. 15. Effect of soil cohesion under various aspect ratios on: (a) active thrust coefficient; (b) normalised height of application point of active thrust to wall base

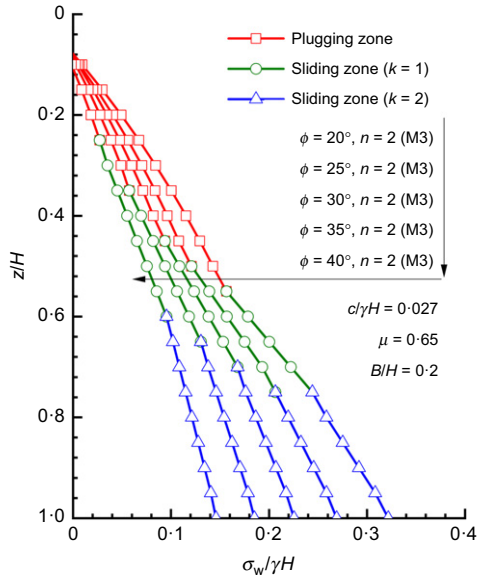

Fig. 16. Effect of soil friction angle on normalised active earth pressure distribution with depth

aspect ratio B/H. For a given B/H and increasing z/H for a retaining wall with narrow cohesive–frictional soil ($B/H < \cot\alpha$), $\sigma_w/\gamma H$ increases non-linearly in the plugging zone and piecewise-linearly in the sliding zone, which is reflected more clearly as follows. There is also a clear increase in the increment rate of $\sigma_w/\gamma H$ when the wall depth changes from the plugging zone to the sliding zone. In addition, $\sigma_w/\gamma H$ increases linearly with z/H when $B/H \geq \cot\alpha$ (with semi-infinite space). Therefore, at a given z/H, $\sigma_w/\gamma H$ increases gradually to a constant value with B/H increasing from 0·1 to a value lower than $\cot\alpha$. This indicates that for a retaining wall with very narrow backfill, using Coulomb's theory with a triangular thrust wedge overestimates greatly the magnitude of the earth pressure and could result in overly conservative designs. Fig. 13 also indicates that when $B/H < \cot\alpha$, for multiple slip surfaces ($n \geq 2$, M3) developed in the sliding zone, a low increment rate of $\sigma_w/\gamma H$ is observed with increasing k at a given n value, this being because the wall–soil interface transfers more vertical stress as the wall depth increases (Handy, 1985). All the above observations show that the direct use of Coulomb's theory without further modifications is inappropriate for estimating accurately the active earth pressure on a retaining wall with narrow soil.

Effect of soil cohesion

Figure 14 presents the effect of the normalised soil cohesion $c/\gamma H$ on the variation of $\sigma_w/\gamma H$ with wall depth z/H. The increase of soil cohesion causes an observable reduction in $\sigma_w/\gamma H$ on the retaining wall at a given z/H. Note that the evolution law for $\sigma_w/\gamma H$ with z/H is the same for different values of soil cohesion, which can be explained as follows: (*a*) the failure mechanisms are associated mainly with the parameters α and n and are unaffected by the soil cohesion; (*b*) in this specific case, the effect of cohesion on shearing forces in soils considered in the analytical framework varies linearly according to the MC failure criterion.

The effects of $c/\gamma H$ on K_a and z_s/H for different values of the aspect ratio are presented in Figs 15(a) and 15(b), respectively. As postulated before, the tensile earth pressure was considered as zero for the calculation. Fig. 15 shows that with increasing $c/\gamma H$, K_a decreases linearly and z_s/H decreases non-linearly, and the variation in z_s/H is more sensitive for very narrow geometries. This implies that considering soil cohesion can yield great savings when designing a retaining wall with a narrow backfill width. It is also evident that Coulomb's solutions neglecting the contribution of cohesion overestimate the design values of $\sigma_w/\gamma H$, K_a and z_s/H.

Effect of soil friction angle

Figure 16 shows the distribution of active earth pressure exerted by narrow cohesive–frictional soil with wall depth for various values of soil friction angle ϕ. As given by equation (2), the heights of the plugging and sliding zones vary with α, which is closely related to ϕ, thus influencing more notably the magnitude and distribution of active earth pressure. At any wall depth, $\sigma_w/\gamma H$ decreases as ϕ increases, the main cause being that higher ϕ yields a stronger soil arching effect. Fig. 16 also shows that higher ϕ leads to a greater reduction in the increment rate of $\sigma_w/\gamma H$ as k increases in the sliding zone.

The variations in the active thrust coefficient K_a and the normalised height of its point of application z_s/H with ϕ for various values of B/H are plotted in Figs 17(a) and 17(b),

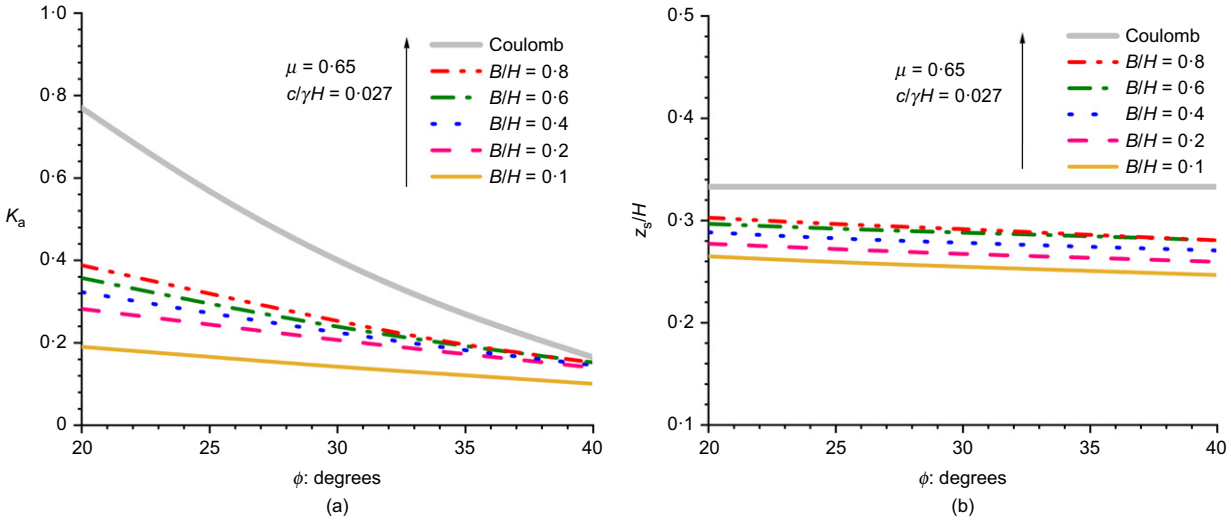

Fig. 17. Effect of soil friction angle under various aspect ratios on: (a) active thrust coefficient; (b) normalised height of application point of active thrust to wall base

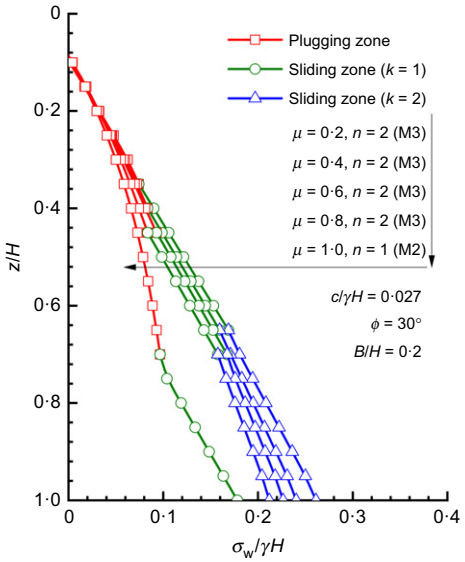

Fig. 18. Effect of wall–soil interface roughness factor on active earth pressure distribution with depth

respectively. As shown in Fig. 17(a), under soil arching, K_a decreases continuously and parabolically with increasing ϕ. Meanwhile, Fig. 17(b) shows that increasing ϕ produces a reduction in z_s/H with a range from around 0·25 to 0·3; this is close to 1/3 as suggested by Coulomb's theory. In addition, for higher ϕ, smaller differences in K_a and z_s/H can be seen when satisfying the geometric condition of $B/H \geq \cot\alpha$, showing that the effect of ϕ weakens in the case of a semi-infinite backfill space.

Effect of wall–soil interface roughness factor

Figure 18 shows the active earth pressure distribution $\sigma_w/\gamma H$ exerted by narrow cohesive–frictional soil with wall depth for various values of roughness factor μ. As can be seen, $\sigma_w/\gamma H$ decreases with increasing μ at a given z/H. This is because the larger friction force acting on the wall–soil interface results in a higher rotation angle of principal stress, further strengthening the soil arching effect on the retaining wall to transfer more vertical stress of the soil. Note that the influence of μ on $\sigma_w/\gamma H$ in the upper zone is very modest because the interface friction-enabled reduction in vertical stress of backfill is a cumulative process from up to down following an exponential function, as can be seen in Handy (1985).

Figures 19(a) and 19(b), respectively, present the variations in active thrust coefficient K_a and normalised height of its point of application z_s/H with μ for various values of B/H. In Fig. 19(a), with increasing μ, earth thrust reduces. However, z_s/H behaves in an opposite way. Both change laws of K_a and z_s/H are more sensitive for narrower backfill. The effect of μ is highly complicated: interestingly, a retaining wall with a rougher interface has a lower earth thrust, but the stability is better for a wall with a smoother interface.

SIMPLIFIED EQUATIONS FOR DESIGN

In practice, using the proposed analytical framework is not as practical as is usually desired because its implementation requires the aid of computer programming. On that basis, a simplified mathematical correlation with the standard Coulomb solution is expected, one that can be used empirically when designing retaining walls with narrow soils. Based on the proposed framework, a modified factor of Coulomb's active earth pressure coefficient (defined as $\beta = K_a/K_{a,\text{Coulomb}}$) and a normalised application height of active thrust (z_s/H) can be provided.

From Table 2, it is the case that for $B/H < \cot\alpha$, either one slip surface with a trapezoid thrust wedge ($n = 1$; M2) or multiple slip surfaces ($n \geq 2$; M3) are likely to occur in narrow soils, whereas it is one slip surface with a triangular wedge rupture body when $B/H \geq \cot\alpha$. To make the design equations usable for retaining walls with narrow soils, B/H must be smaller than 0·6 according to Table 2. In total, 625 groups of calculated β and z_s/H in narrow backfills with varying aspect ratio (B/H = 0·1, 0·2, 0·3, 0·4, 0·5), soil cohesion ($c/\gamma H$ = 0·00, 0·01, 0·02, 0·03, 0·04), soil friction angle (ϕ = 20°, 25°, 30°, 35°, 40°) and roughness factor of wall–soil interface (μ = 0·2, 0·4, 0·6, 0·8, 1) are generated as the dataset using the proposed framework. On this basis, two simplified approximations in terms of β and z_s/H are then proposed using curve fitting, as

$$\beta = p_1 + p_2\frac{B\tan\phi}{H} + p_3\frac{\mu B}{H} + p_4\frac{cB}{\gamma H^2} + p_5\mu\tan\phi + p_6\mu \quad (47)$$

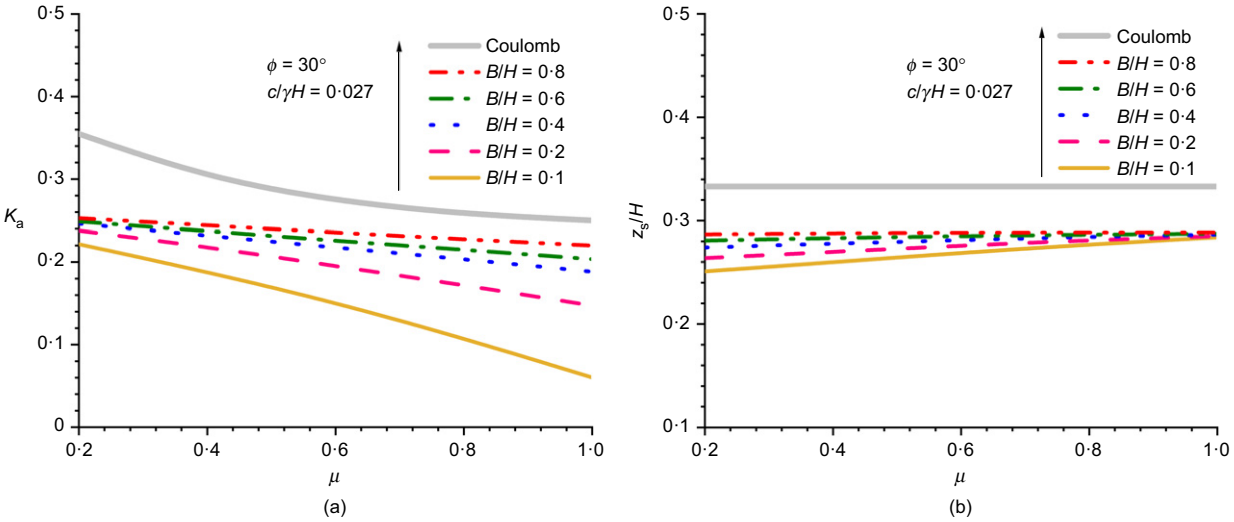

Fig. 19. Effect of wall–soil interface roughness factor under various aspect ratios on: (a) active thrust coefficient; (b) normalised height of application point of active thrust to wall base

Table 3. Optimal value of constant coefficients for closed-form approximation

p_1	p_2	p_3	p_4	p_5	p_6	p_7	p_8	p_9	p_{10}	p_{11}
0·965	0·403	2·338	−25·44	−0·037	−0·771	0·335	0·05	−2·421	−0·291	−0·023

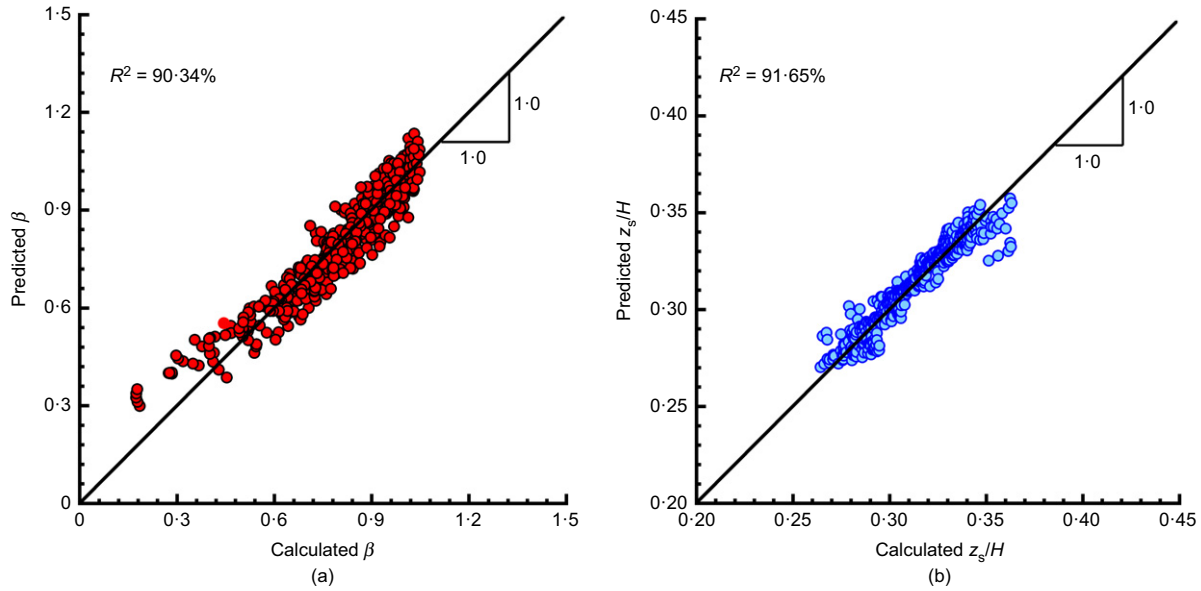

Fig. 20. Predicted values from the simplified design equations plotted against calculated values from the proposed framework: (a) modified factor β; (b) normalised height of application point of active thrust z_s/H

$$\frac{z_s}{H} = p_7 + p_8 \mu \tan\phi + p_9 \frac{c\tan\phi}{\gamma H} + p_{10}\frac{\mu c}{\gamma H} + p_{11}\frac{B}{H} \qquad (48)$$

where p_1 to p_{12} are optimal constant coefficients for the closed-form approximations, as listed in Table 3.

The comparisons of β and z_s/H between the predicted data from the design equations and the calculated data from the proposed framework are shown in Figs 20(a) and 20(b), respectively. As can be seen, the design equations agree well with the proposed analytical framework, with coefficients of determination (R^2) of up to 90·34% and 91·65%, respectively.

The given design equations consider comprehensively soil cohesion, soil arching, horizontal shearing forces in narrow backfills and complex failure patterns. In design practice, determining β and z_s/H is very simple and quick because only four dimensionless parameters B/H, $c/\gamma H$, $\tan\phi$ and μ are required as inputs for equations (47) and (48).

As demonstrated in Fig. 20(a), the proposed analytical solution for narrow retained soils gives lower active earth pressure values than does the standard Coulomb theory ($\beta < 1{\cdot}0$), particularly so for some extreme cases with higher soil strength parameters (soil cohesion and/or friction angle)

and/or wall–soil interface roughness factor. These cases would require careful safety consideration because some occasional conditions in practice may lead to higher active pressure – for example, vibrations during construction and unrealistic estimation of wall friction and soil strength. To avoid these safety risks, a moderate reduction factor in soil strength parameters and/or wall–soil interface roughness factor or a lower bound on the modified factor β (e.g. $\beta \leqslant 0{\cdot}5$) may be applied. More importantly, all these possibilities must be examined thoroughly by means of experiments or field observations before using the simplified equations in industry, which is clearly beyond the present scope.

Although the simplified design equations have been presented here, some limitations must be clarified before putting them into practice. Advocating design based on extremely low earth pressures from the simplified equations for retaining walls with limited space requires the walls to displace outwards (away from the soil), such as in confined excavations. In addition, even though a full tension cut-off has been considered in the simplified design equations to address negative earth pressures, the proposed solutions can only be used as a lower bound of the earth pressure for a displacing wall because of the assumptions used in the derivations. For a rigid wall that does not displace, the at-rest pressure should be recommended primarily in the case of some loading conditions such as freezing/thawing cycles, wetting cycles or vibrations.

CONCLUSIONS

This study has presented a generalised analytical framework for active earth pressure calculations of retaining walls with limited backfill space considering soil cohesion, soil arching effect, horizontal shearing forces and complex failure. The analytical solution combined a newly developed ADE method and a sliding wedge method. Complex soil failure (e.g. multiple failure surface) was observed in FELA models. A full tension cut-off criterion was used to consider the effect of soil cohesion. Because the proposed framework involves the load transfer mechanisms and failure mechanisms as much as possible, it is more realistic than the traditional Coulomb earth pressure theory. A series of parametric studies revealed the effects of aspect ratio (B/H), soil strength parameters (c and ϕ) and wall–soil interface roughness factor (μ) on active earth pressure, active thrust and its application height. Equations for calculating a modified active earth pressure coefficient and an application height of active thrust were provided for using the framework directly for design under certain conditions. The main findings are given below.

(*a*) The failure modes that develop in narrow soils present various slip surface numbers and shapes depending on the combined effects of aspect ratio, soil friction angle and wall–soil interface friction angle, but barely affected by soil cohesion. For $B/H \geq \cot\alpha$, one slip surface forms with a triangular thrust wedge; for $B/H < \cot\alpha$, one slip surface with a trapezoidal thrust wedge might develop, and multiple slip surfaces develop as reflections in backfills with very narrow width.

(*b*) For one slip surface with a triangular thrust wedge, the active earth pressure increases linearly with wall depth. For one slip surface with a trapezoidal thrust wedge and multiple slip surfaces, the active earth pressure increases non-linearly in the upper plugging zone and piecewise-linearly in the lower sliding zone, and it shows an obvious increase in increment rate when the retained soil varies from the plugging zone to the sliding zone; moreover, changes in the increment rate of earth pressure occur in the sliding zone with the transition of multiple slip surfaces from top to bottom.

(*c*) For a given aspect ratio, the higher the soil cohesion and the soil friction angle, the lower the active thrust and the height of its application point from the wall base, indicating the stronger stability against overturning of a retaining wall system with narrow soil. A larger wall–soil interface roughness factor helps to reduce the earth pressure and thrust but may increase the application height.

Although a more generalised analytical framework has been proposed, some limitations are still worth investigating further; for example, some specific cases of retaining walls with inclined back faces were not considered, nor was the discrepancy in interfacial behaviour on either side of a retaining structure built near a rock face. Nevertheless, the proposed analytical framework provides a basis for conducting more sophisticated analyses considering the non-linear behaviour of the wall–soil interface, various wall movement modes (e.g. rotation about the base, the top or a combination with translation) and the inclined angle of retaining wall back faces. Also, the proposed analytical framework offers good guidance for the practical design of retaining walls with narrow soils.

ACKNOWLEDGEMENTS

This work was financially supported by the National Natural Science Foundation of China (grant no. 41972269). The first author was supported by a CSC grant. The authors express their great appreciation to Associate Professor Franz Tschuchnigg at Graz University of Technology for his invaluable suggestions on the use of FELA and finite-element modelling programs, as well as the Davis approach.

NOTATION

a	abbreviation used in derivation process
B	width of narrow soil
B_n	width of sliding wedge W_{n1} at top
C_1 to C_5	abbreviations used in derivation process
C_{nk}	resultant cohesion along wall–soil interface or slip surface
c	soil cohesion
c^*	reduced soil cohesion using Davis approach
E_a	active thrust
E_a^i	resultant active earth pressure exerted by soil slice
E_{nk}	resultant earth pressure on retaining wall for sliding wedges
F_z	total vertical force on top of lower zone
$F_z^{AA'}$ and $F_z^{CC'}$	vertical forces on lateral boundaries of arched soil layer element
F_z^{AC} and $F_z^{A'C'}$	vertical forces on upper and lower boundaries of arched soil layer element
G	gravity of arched soil layer element
G_{nk}	gravity of sliding wedge W_{nk}
H	retaining wall depth
H_0	height of non-yielding zone
H_{nk}	height of real slip surface
h_{nk}	height of hypothetical slip surface
i	ith soil slice
K_a and $K_{a,Coulomb}$	active thrust coefficient from proposed solution and Coulomb theory
k	kth slip surface formed in yielding zone
l_{arcAC}	arc length of arched soil layer element
m	division number of soil slices
N	ratio of major to minor principal stresses
n	number of total slip surfaces formed in yielding zone
R_{AC} and $R_{A'C'}$	radii of minor principal stress trajectory
R_{nk}	force normal to slip surface for sliding wedges

W_{nk} number of sliding wedges
z arbitrary wall depth
z_s application point of active thrust from wall base
α sliding angle of slip surface
γ unit weight
Δz thickness of soil slice
Δz_{Ai} vertical distance between points A and i
δ wall–soil interface friction angle
θ_w and θ_i rotation angles of principal stress on wall and at any position of element
μ wall–soil interface roughness factor
σ_1^0 and σ_1^i major principal stresses on wall and at any position of element
σ_3^0 and σ_3^i minor principal stresses on wall and at any position of element
σ_v^0 and σ_v^i vertical stresses on wall and at any position of element
$\bar{\sigma}_{v0}$ average uniform vertical stress on top of lower zone
σ_w^u and σ_w^l earth pressures in upper and lower zones
σ_{wi}^l active earth pressure exerted by soil slice of lower zone
τ_s and τ_w shear strengths of retained soil and wall–soil interface
φ soil friction angle
ϕ^* reduced soil friction angle using Davis approach
ψ soil dilation angle

REFERENCES

Cao, W., Zhang, H., Liu, T. & Tan, X. (2020). Analytical solution for the active earth pressure of cohesionless soil behind an inclined retaining wall based on the curved thin-layer element method. *Comput. Geotech.* **128**, 103851.

Chen, R., Meng, F., Li, Z., Ye, Y. & Ye, J. (2016). Investigation of response of metro tunnels due to adjacent large excavation and protective measures in soft soils. *Tunn. Undergr. Space Technol.* **58**, 224–235.

Chen, J. J., Li, M. G. & Wang, J. H. (2017). Active earth pressure against rigid retaining walls subjected to confined cohesionless soil. *Int. J. Geomech.* **17**, No. 6, 06016041.

Chen, F., Lin, Y. & Li, D. (2019). Solution to active earth pressure of narrow cohesionless backfill against rigid retaining walls under translation mode. *Soils Found.* **59**, No. 1, 151–161.

Davis, E. (1968). Theories of plasticity and failures of soil masses. In *Soil mechanics: selected topics* (ed. I. K. Lee), pp. 341–354. New York, NY, USA: Elsevier.

Fan, C. C. & Fang, Y. S. (2010). Numerical solution of active earth pressures on rigid retaining walls built near rock faces. *Comput. Geotech.* **37**, No. 7–8, 1023–1029.

Frydman, S. & Keissar, I. (1987). Earth pressure on retaining walls near rock faces. *J. Geotech. Engng* **113**, No. 6, 586–599.

Greco, V. (2013). Active thrust on retaining walls of narrow backfill width. *Comput. Geotech.* **50**, 66–78.

Handy, R. L. (1985). The arch in soil arching. *J. Geotech. Engng* **111**, No. 3, 302–318.

Janssen, H. A. (1895). Versuche über Getreidedruck in Silozellen. *Zeitschrift VDI* **39**, 1045–1049 (in German).

Krabbenhoft, K., Lyamin, A. & Krabbenhoft, J. (2015). *Optum G2*. Copenhagen, Denmark: Optum Computational Engineering. See https://optumce.com/products/optumg2/ (accessed 09/11/2022).

Li, M. G., Chen, J. J. & Wang, J. H. (2017). Arching effect on lateral pressure of confined granular material: numerical and theoretical analysis. *Granul. Matter* **19**, No. 2, article 20.

Liu, F. & Wang, J. (2008). A generalized slip line solution to the active earth pressure on circular retaining walls. *Comput. Geotech.* **35**, No. 2, 155–164.

O'Neal, T. S. & Hagerty, D. (2011). Earth pressures in confined cohesionless backfill against tall rigid walls – a case history. *Can. Geotech. J.* **48**, No. 8, 1188–1197.

Paik, K. H. & Salgado, R. (2003). Estimation of active earth pressure against rigid retaining walls considering arching effects. *Géotechnique* **53**, No. 7, 643–653, https://doi.org/10.1680/geot.2003.53.7.643.

Schmüdderich, C., Tschuchnigg, F. & Schweiger, H. F. (2022). Significance of flow rule for the passive earth pressure problem. *Acta Geotech.* **17**, 81–92.

Sheil, B. & Templeman, J. (2022). Bearing capacity of open caissons embedded in sand. *Géotechnique*, https://doi.org/10.1680/jgeot.21.00089.

Sloan, S. (2013). Geotechnical stability analysis. *Géotechnique* **63**, No. 7, 531–571, https://doi.org/10.1680/geot.12.RL.001.

Take, W. & Valsangkar, A. (2001). Earth pressures on unyielding retaining walls of narrow backfill width. *Can. Geotech. J.* **38**, No. 6, 1220–1230.

Terzaghi, K. (1943). *Theoretical soil mechanics*. New York, NY, USA: John Wiley and Sons.

Tschuchnigg, F., Schweiger, H., Sloan, S. W., Lyamin, A. V. & Raissakis, I. (2015). Comparison of finite-element limit analysis and strength reduction techniques. *Géotechnique* **65**, No. 4, 249–257, https://doi.org/10.1680/geot.14.P.022.

Tu, B. X. & Jia, J. Q. (2014). Active earth pressure from c–φ soil backfill. *Proc. Instn Civ. Engrs Geotech. Engng* **167**, No. 3, 270–280, https://doi.org/10.1680/geng.12.00008.

Wang, Y. Z. (2000). Distribution of earth pressure on a retaining wall. *Géotechnique* **50**, No. 1, 83–88, https://doi.org/10.1680/geot.2000.50.1.83.

Xie, Y. & Leshchinsky, B. (2016). Active earth pressures from a log-spiral slip surface with arching effects. *Géotech. Lett.* **6**, No. 2, 149–155, https://doi.org/10.1680/jgele.16.00015.

Zhu, D. Y. & Qian, Q. (2000). Determination of passive earth pressure coefficients by the method of triangular slices. *Can. Geotech. J.* **37**, No. 2, 485–491.